

This version of the article has been accepted for publication, after a peer-review process, and is subject to Springer Nature's AM terms of use, but is not the Version of Record and does not reflect post-acceptance improvements, or any corrections. The Version of Record is available online at: <https://doi.org/10.1007/s10915-015-0043-2>

High order boundary extrapolation technique for finite difference methods on complex domains with Cartesian meshes

A. Baeza · P. Mulet · D. Zorío

Abstract The application of suitable numerical boundary conditions for hyperbolic conservation laws on domains with complex geometry has become a problem with certain difficulty that has been tackled in different ways according to the nature of the numerical methods and mesh type. In this paper we present a technique for the extrapolation of information from the interior of the computational domain to ghost cells designed for structured Cartesian meshes (which, as opposed to non-structured meshes, cannot be adapted to the morphology of the domain boundary).

This technique is based on the application of Lagrange interpolation with a filter for the detection of discontinuities that permits a data dependent extrapolation, with higher order at smooth regions and essentially non oscillatory properties near discontinuities.

Keywords Finite difference WENO schemes, Cartesian grids, extrapolation.

1 Introduction

Hyperbolic conservation laws and related equations have been the focus of many research lines in the past four decades. Since no analytic solution is known for many of these equations, different techniques have been developed in order to tackle these problems from a numerical point of view, with methodologies that have evolved and improved along these years.

Some of these methods, mainly used for academic purposes, employ Cartesian meshes on rectangular domains and numerical boundary conditions that are based on low order extrapolation, generally first order. Due to the advantages of implementation and efficiency inherent to Cartesian meshes, in our case we will focus on extending the techniques mentioned above to domains with complex geometry (i.e., at least not necessarily rectangular). We will also present a new technique for the extrapolation of interior information to ghost cells (cells outside the domain, but within the stencils of interior points) making use of boundary conditions (if

Departament de Matemàtica Aplicada, Universitat de València (Spain); emails: antonio.baeza@uv.es, mulet@uv.es, david.zorio@uv.es. This research was partially supported by Spanish MINECO grants MTM2011-22741 and MTM2014-54388.

available) and interior data near a given ghost cell. This procedure is able to detect abrupt data changes.

Some authors have approached this problem from different perspectives. In [19] the authors develop a technique based on Lagrange interpolation with a limiter which is restricted to second order methods and a single ghost cell. Also related to our approach are the works of Shu and collaborators [20, 21] where the equation to be solved is used to extrapolate derivative values of the numerical solution to the boundary points where inflow conditions are prescribed and then approximate ghost values by a Taylor expansion. For outflow boundaries an extrapolation technique based on the WENO method is used, achieving high order when the data is smooth in both cases. The drawbacks of this approach are that it is problem-dependent (see [12, 23] for a similar methodology applied to other equations), that it requires a different treatment of different types of boundary and its relatively high computational cost.

Our approach can be understood as an extension of [19] in the sense that it is based on Lagrange extrapolation with filters, but without imposing limitations on the order of the method or the number of ghost cells. Further, albeit the description is made for hyperbolic conservation laws, the procedure is agnostic about the equation and can be applied to other hyperbolic problems. Finally, the methodology is the same for inflow and outflow boundaries, just by considering the boundary node as an interpolation node in the case of inflow data.

The organization of the paper is the following: In section 2 we present the equations and the numerical methods that we consider in this paper. The details of the procedure for meshing complex domains with Cartesian meshes are explained in section 3. In section 4 we expound how we perform extrapolations with the method for the detection of singularities. Some numerical results that are obtained with this methodology are presented in section 5, with some simple tests in 1D to illustrate the correct behavior of the proposed techniques and some more complex ones in 2D. Finally, some conclusions are drawn in section 6.

2 Numerical schemes

The equations that will be considered throughout this paper are hyperbolic systems of m two-dimensional conservation laws

$$u_t + f(u)_x + g(u)_y = 0, \quad u = u(x, y, t), \quad (1)$$

defined on an open and bounded spatial domain $\Omega \subseteq \mathbb{R}^2$, with Lipschitz boundary $\partial\Omega$ given by a finite union of piece-wise smooth curves, $u : \Omega \times \mathbb{R}^+ \rightarrow \mathbb{R}^m$, and fluxes $f, g : \mathbb{R}^m \rightarrow \mathbb{R}^m$. These equations are supplemented with an initial condition, $u(x, y, 0) = u_0(x, y)$, $u_0 : \Omega \rightarrow \mathbb{R}^m$, and different boundary conditions that may vary depending on the problem.

2.1 Finite difference WENO schemes

Although the techniques that will be expounded in this paper are applicable to other numerical schemes, we use here Shu-Osher's finite difference conservative methods [18] with a WENO5 (*Weighted Essentially Non-Oscillatory*) [13] spatial

reconstruction, Donat-Marquina's flux-splitting [7] and the RK3-TVD ODE solver [17] in a method of lines fashion that we briefly describe here for the sake of completeness. This combination of techniques was proposed in [14].

We define our mesh starting from a reference vertical line, $x = \bar{x}$ and a horizontal one $y = \bar{y}$. Let $h_x > 0$ and $h_y > 0$ be the horizontal and vertical spacings of the mesh, so that the vertical lines in the mesh are determined by: $x = x_r := \bar{x} + rh_x$, $r \in \mathbb{Z}$ and the horizontal ones by $y = y_s := \bar{y} + sh_y$, $s \in \mathbb{Z}$. The cell with center (x_r, y_s) is defined by:

$$[x_r - \frac{h_x}{2}, x_r + \frac{h_x}{2}] \times [y_s - \frac{h_y}{2}, y_s + \frac{h_y}{2}].$$

The computational domain is then given by

$$\mathcal{D} := \{(x_r, y_s) : (x_r, y_s) \in \Omega, \quad r, s \in \mathbb{Z}\} = (\bar{x} + h_x \mathbb{Z}) \times (\bar{y} + h_y \mathbb{Z}) \cap \Omega.$$

Notice that \mathcal{D} is finite since Ω is bounded.

Shu and Osher's technique [17] to obtain high order finite difference schemes relies on the fact that, for fixed y, t :

$$f(u)_x(x, y, t) = \frac{1}{h_x} \left(\varphi(x + \frac{h_x}{2}, y, t) - \varphi(x - \frac{h_x}{2}, y, t) \right),$$

for and implicitly defined $\varphi = \varphi^{h_x}$ that satisfies

$$f(u(x, y, t)) = \frac{1}{h_x} \int_{x - \frac{h_x}{2}}^{x + \frac{h_x}{2}} \varphi(\xi, y, t) d\xi.$$

We can compute highly accurate approximations to $\varphi(x_{i \pm \frac{1}{2}}, y_j, t)$, denoted by $\hat{\varphi}(x_{i \pm \frac{1}{2}}, y_j, t)$, using known grid values of $f(u)$ as

$$\begin{aligned} \varphi(x_{i + \frac{1}{2}}, y_j, t) &= \hat{\varphi}(x_{i + \frac{1}{2}}, y_j, t) + \mathcal{O}(h_x^r), \\ \hat{\varphi}(x, y_j, t) &= \mathcal{R}(f_{i-p,j}(t), \dots, f_{i+q,j}(t); x), \quad f_{l,j}(t) = f(u(x_l, y_j, t)), \end{aligned}$$

where \mathcal{R} is a reconstruction procedure (a function whose cell-averages coincide with the given ones; we use the WENO technique proposed in [13, 1] for five points stencils). We can thus discretize the spatial derivative in (1) as:

$$\begin{aligned} (f(u))_x(x_i, y_j, t) &= \frac{\hat{f}_{i+\frac{1}{2},j}(t) - \hat{f}_{i-\frac{1}{2},j}(t)}{h_x} + \mathcal{O}(h_x^r), \\ \hat{f}_{i+\frac{1}{2},j}(t) &= \hat{\varphi}(x_{i+\frac{1}{2}}, y_j, t) = \hat{f}(u(x_{i-p}, y_j, t), \dots, u(x_{i+q}, y_j, t)). \end{aligned} \quad (2)$$

Similarly

$$(g(u))_y(x_i, y_j, t) = \frac{\hat{g}_{i,j+\frac{1}{2}}(t) - \hat{g}_{i,j-\frac{1}{2}}(t)}{h_y} + \mathcal{O}(h_y^r). \quad (3)$$

The numerical approximations in (2) and (3) must be modified when some of the nodes involved in their computations are not in Ω . As we will detail in section 3 and 4, we use extrapolation from interior data and possible boundary conditions to obtain approximations

$$\tilde{u}(x_r, y_s, t) = u(x_r, y_s, t) + \mathcal{O}(h_x^s), \quad (4)$$

for $(x_r, y_s) \notin \Omega$, should u be defined and smooth enough at an open set containing the stencil involved in the extrapolation and the evaluation point (x_r, y_s) . For the sake of the exposition, let us assume that in (2) $(x_{i-p-1}, y_j) \notin \Omega$ and $(x_{i-p}, y_j), \dots, (x_{i+q}, y_j) \in \Omega$ and denote by $v_r = u(x_r, y_j, t)$, $\tilde{v}_r = \tilde{u}(x_r, y_j, t)$. Then the approximation in (2) that corresponds to the numerical scheme with the extrapolated value $\tilde{u}(x_{i-p-1}, y_j, t)$ satisfies, under mild smoothness conditions,

$$\begin{aligned} & \frac{\hat{f}(v_{i-p}, \dots, v_{i+q}) - \hat{f}(\tilde{v}_{i-p-1}, \dots, v_{i+q-1})}{h_x} \\ &= \frac{\hat{f}(v_{i-p}, \dots, v_{i+q}) - \hat{f}(v_{i-p-1}, \dots, v_{i+q-1})}{h_x} + \mathcal{O}(h_x^{s-1}) \\ &= (f(u))_x(x_i, y_j, t) + \mathcal{O}(h_x^{r'}), \quad (5) \end{aligned}$$

with $r' = \min(r, s-1)$, as it will be seen in Appendix C. The same conclusion holds if other arguments are replaced by suitable extrapolations. We will see in the numerical experiments how the choice of s affects the accuracy of the solution. The issue of stability of the scheme with extrapolation at the boundary will be tackled in Appendix B in a simple one-dimensional setup that will serve as guide for the design of the multidimensional extension of extrapolation.

The spatial discretization of problem (1) reads as:

$$\begin{aligned} u'_{i,j}(t) &= -\mathcal{L}(u(t))_{i,j}, \quad u_{i,j} = [u_{1,i,j}, \dots, u_{m,i,j}]^T, \\ \mathcal{L}(u)_{i,j} &= g \frac{\hat{f}_{i+\frac{1}{2},j} - \hat{f}_{i-\frac{1}{2},j}}{h_x} + \frac{\hat{g}_{i,j+\frac{1}{2}} - \hat{g}_{i,j-\frac{1}{2}}}{h_y}, \end{aligned}$$

for approximations $u_{i,j}(t) \approx u(x_i, y_j, t)$ and it can be solved using an appropriate ODE solver. In this paper, we use the third order TVD Runge-Kutta scheme proposed in [17]:

$$\begin{cases} u^{(1)} = u^n - \Delta t \mathcal{L}(u^n), \\ u^{(2)} = \frac{3}{4}u^n + \frac{1}{4}u^{(1)} - \frac{1}{4}\Delta t \mathcal{L}(u^{(1)}), \\ u^{n+1} = \frac{1}{3}u^n + \frac{2}{3}u^{(2)} - \frac{2}{3}\Delta t \mathcal{L}(u^{(2)}), \end{cases} \quad (6)$$

for $u_{i,j}^n \approx u_{i,j}(t_n) \approx u(x_i, y_j, t_n)$.

To extend these schemes to systems of conservation laws we can compute the numerical flux $\hat{f}_{i+\frac{1}{2}}$ (we drop the j subscript for simplicity) by using a fifth order Donat-Marquina's flux-splitting [7]:

$$\begin{aligned} \hat{f}_{i+\frac{1}{2}} &= \sum_{k=1}^m r^{+,k} \left(\mathcal{R}^+ \left(l^{+,k} \cdot f_{i-2}^{+,k}, \dots, l^{+,k} \cdot f_{i+2}^{+,k}; x_{i+\frac{1}{2}} \right) \right) \\ &+ \sum_{k=1}^m r^{-,k} \left(\mathcal{R}^- \left(l^{-,k} \cdot f_{i-1}^{-,k}, \dots, l^{-,k} \cdot f_{i+3}^{-,k}; x_{i+\frac{1}{2}} \right) \right), \end{aligned} \quad (7)$$

where $f_l^{\pm,k} = f^{\pm,k}(u_l)$ as defined below, $r^{\pm,k} = r^k(u_{i+\frac{1}{2}}^{\pm})$, $l^{\pm,k} = l^k(u_{i+\frac{1}{2}}^{\pm})$ are the right and left normalized eigenvectors corresponding to the eigenvalue $\lambda_k(f'(u_{i+\frac{1}{2}}^{\pm}))$ of the flux Jacobian $f'(u_{i+\frac{1}{2}}^{\pm})$, respectively, computed at $u_{i+\frac{1}{2}}^{\pm}$, where

$$u_{i+\frac{1}{2}}^+ = \mathcal{I}^+(u_{i-2}, \dots, u_{i+2}; x_{i+\frac{1}{2}}), \quad u_{i+\frac{1}{2}}^- = \mathcal{I}^-(u_{i-1}, \dots, u_{i+3}; x_{i+\frac{1}{2}}),$$

for some interpolators I^\pm . The functions $f^{\pm,k}$ satisfy $f^{+,k} + f^{-,k} = f$, $\pm \lambda_k((f^{\pm,k})'(u)) > 0$ for u in some relevant range $\mathcal{M}_{i+\frac{1}{2}}$ near $u_{i+\frac{1}{2}}^\pm$, and are given by:

$$(f^{-,k}, f^{+,k})(v) = \begin{cases} (0, f(v)) & \lambda_k(f'(u)) > 0, \quad \forall u \in \mathcal{M}_{i+\frac{1}{2}} \\ (f(v), 0) & \lambda_k(f'(u)) < 0, \quad \forall u \in \mathcal{M}_{i+\frac{1}{2}} \\ (\frac{1}{2}(f(v) - \alpha_{i+\frac{1}{2}}^k v), \frac{1}{2}(f(v) + \alpha_{i+\frac{1}{2}}^k v)), & \exists u \in \mathcal{M}_{i+\frac{1}{2}} / \lambda_k(f'(u)) = 0, \end{cases}$$

where $\alpha_{i+\frac{1}{2}}^k \geq |\lambda_k(f'(u))|$ for $u \in \mathcal{M}_{i+\frac{1}{2}}$. For the Euler equations we can simply take $\mathcal{M}_{i+\frac{1}{2}} = \{u_i, u_{i+1}\}$.

3 Meshing procedure

3.1 Ghost cells

We recall that WENO schemes of order $2k-1$ use an stencil (consecutive indexes) of $2k$ points, therefore k additional cells are needed at both sides of each horizontal and vertical mesh line in order to perform a time step. These additional cells are usually named *ghost cells* and, in terms of their centers, are given by:

$$\mathcal{GC} := \mathcal{GC}_x \cup \mathcal{GC}_y,$$

where

$$\mathcal{GC}_x := \{(x_r, y_s) : 0 < d(x_r, \Pi_x(\mathcal{D} \cap (\mathbb{R} \times \{y_s\}))) \leq kh_x, \quad r, s \in \mathbb{Z}\},$$

$$\mathcal{GC}_y := \{(x_r, y_s) : 0 < d(y_s, \Pi_y(\mathcal{D} \cap (\{x_r\} \times \mathbb{R}))) \leq kh_y, \quad r, s \in \mathbb{Z}\},$$

where Π_x and Π_y denote the projections on the respective coordinates and,

$$d(a, B) := \inf\{|b - a| : b \in B\},$$

for given $a \in \mathbb{R}$ and $B \subseteq \mathbb{R}$. Notice that $d(a, \emptyset) = +\infty$, since, by convention, $\inf \emptyset = +\infty$.

3.2 Normal lines

The extrapolation procedure in 1D can be reasonably performed after the accuracy and stability analysis that have been performed in Section 2 and Appendix B. We focus now on the two-dimensional setting and boundaries with prescribed Dirichlet conditions, e.g., reflective boundary conditions for the Euler equations. In this situation, it seems reasonable that the extrapolation at a certain ghost cell $c_* = (x_*, y_*)$ be based on the prescribed value at the nearest boundary point. It can be proven that a point $p \in \partial\Omega$ satisfying

$$\|c_* - p\|_2 = \min\{\|c_* - p'\|_2 : p' \in \partial\Omega\}$$

also satisfies that the line determined by c_* and p is normal to the curve $\partial\Omega$ at p , if $\partial\Omega$ is differentiable at p . Uniqueness of p holds whenever c_* is close enough to the boundary, so we will henceforth denote $N(c_*) = p$.

This argument suggests that a good strategy is to perform a (virtual) rotation of the domain and obtain data on some points $N_i \in \Omega$ on the line that passes through c_* and $N(c_*)$ (normal line to $\partial\Omega$ passing by c_*) (see Subsection 3.2.1 for the details on this choice) and then use a one-dimensional extrapolation from the data on these points on the segment to approximate the value at c_* .

In case that the boundary conditions prescribe values for the normal component of a vectorial unknown \vec{v} related to the coordinates frame (as is the case for reflective boundary conditions for the Euler equations), then one defines

$$\vec{n} = \frac{c_* - N(c_*)}{\|c_* - N(c_*)\|}, \quad \vec{t} = \vec{n}^\perp,$$

and obtains normal and tangential components of \vec{v} at each point N_i of the mentioned segment by:

$$v^t(N_i) = \vec{v}(N_i) \cdot \vec{t}, \quad v^n(N_i) = \vec{v}(N_i) \cdot \vec{n}.$$

The extrapolation procedure is applied to $v^t(N_i)$ to approximate $v^t(c_*)$ and to $v^n(N_i)$ and $v^n(N(c_*)) = 0$ to approximate $v^n(c_*)$. Once $v^t(c_*)$, $v^n(c_*)$ are approximated, the approximation to $\vec{v}(c_*)$ is set to

$$\vec{v}(c_*) = v^t(c_*)\vec{t} + v^n(c_*)\vec{n}.$$

3.2.1 Choice of nodes on normal lines

As mentioned in Section 2, if we wish to formally preserve a certain precision in the resulting scheme, it is necessary to extrapolate the information from the interior of the domain in an adequate manner. Therefore, if the basic numerical scheme has order r it is reasonable to use extrapolation of this order at least. For the sake of clarity, we will not distinguish between interpolation or extrapolation when these take place at the interior of the domain.

At this point there are many possibilities. However, as expected, not all of them yield the same quality in the results nor the same computational efficiency. The following configuration supposes a reasonable balance between both previous factors.

We proceed in a similar fashion as in [19]. Let $(x_*, y_*) \in \mathcal{GC}$ and consider the corresponding point in $\partial\Omega$ at minimal distance, $N(x_*, y_*)$. As already mentioned, the vector determined by both points is orthogonal to $\partial\Omega$ at $N(x_*, y_*)$. Let us suppose that we wish to use an extrapolation of order r at the ghost cell center (x_*, y_*) .

At first place, one needs to obtain data from the information in \mathcal{D} at a set of points $\mathcal{N}(x_*, y_*) = \{N_1, \dots, N_R\}$, with $R \geq r$, on the line determined by the points (x_*, y_*) and $N(x_*, y_*)$. By a CFL stability motivation (see Appendix B for further details), we will do the selection with a spacing between them of at least the distance between (x_*, y_*) and $N(x_*, y_*)$. We will go further into this issue in section 5. We will choose the nodes depending on the slope of the normal line, so that the use of interior information is maximized. We will henceforth denote by $E(x)$ the integer rounding of x towards ∞ , i.e., $\text{sign}(E(x)) = \text{sign}(x)$ and $|E(x)| = \min(\mathbb{N} \cap [|x|, \infty))$.

We denote by $v = (v_1, v_2)$ the vector determined by (x_*, y_*) and $N(x_*, y_*)$, so that the normal line passing through (x_*, y_*) is given by the parametric equations:

$$\begin{aligned} x &= x_* + sv_1 \\ y &= y_* + sv_2. \end{aligned}$$

Depending on the angle θ of the vector $v = (v_1, v_2)$, we consider two possibilities:

1. $|v_1| \geq |v_2|$.
2. $|v_1| < |v_2|$.

In the first case we take points $N'_q = (x_* + qC_x h_x, y_* + qC_x h_x \frac{v_2}{v_1})$, with $C_x \in \mathbb{Z}$ chosen with the same sign as v_1 and so that:

$$\begin{aligned} \|N'_q - N'_{q+1}\|_2 &\geq \|v\|_2 \\ \|N'_q - N'_{q+1}\|_2 &= \frac{h_x |C_x|}{|v_1|} \|v\|_2 \geq \|v\|_2 \Leftrightarrow |C_x| \geq \frac{|v_1|}{h_x}. \end{aligned}$$

Therefore, our choice is $C_x = E(\frac{v_1}{h_x})$.

Now, if Dirichlet boundary conditions at $N(x_*, y_*)$ are prescribed, we take the nodes

$$\mathcal{N}(x_*, y_*) = \{N(x_*, y_*), N'_2, \dots, N'_{R+1}\}, \quad (8)$$

i.e., we drop N'_1 from the list. If no boundary condition is specified on $N(x_*, y_*)$ then

$$\mathcal{N}(x_*, y_*) = \{N'_1, N'_2, \dots, N'_R\}. \quad (9)$$

In this fashion, the chosen nodes $\mathcal{N}(x_*, y_*) = \{N_1, \dots, N_R\}$ satisfy $\|N_q - N_{q+1}\|_2 \geq \|v\|_2$, $q = 1, \dots, R-1$.

Denote $N_q = (\tilde{x}_q, \tilde{y}_q)$. For each q for which $u(\tilde{x}_q, \tilde{y}_q)$ is not known, we need to obtain a sufficiently accurate approximation of this value from the information on the interior nodes. Since the second coordinate, \tilde{y}_q , of N_q does not need to coincide with the center of a vertical cell, we will use interpolation from the cells in the line $x = \tilde{x}_q$ by using the following set of points:

$$\begin{aligned} \mathcal{S}_q &= \{N_{q,1}, \dots, N_{q,R}\} := \operatorname{argmin}_{A \in \mathcal{A}} \sum_{(\tilde{x}_q, y_s) \in A} |y_s - \tilde{y}_q|, \\ \mathcal{A} &:= \{A = \{(\tilde{x}_q, y_j), \dots, (\tilde{x}_q, y_{j+R-1})\} / A \subseteq \mathcal{D}\}. \end{aligned}$$

That is, we select the vertical stencil of length R with a first coordinate fixed to \tilde{x}_q such that it be as centered as possible with respect to the point N_q , see Figure 1 (a) for a graphical example.

In a dual fashion, in the second case we take points $N_q = (x_* + qC_y h_y \frac{v_1}{v_2}, y_* + qC_y h_y)$, with $C_y = E(\frac{v_2}{h_y})$ and

$$\begin{aligned} \mathcal{S}_q &= \{N_{q,1}, \dots, N_{q,R}\} := \operatorname{argmin}_{A \in \mathcal{A}} \sum_{(x_s, \tilde{y}_q) \in A} |x_s - \tilde{x}_q|, \\ \mathcal{A} &:= \{A = \{(x_j, \tilde{y}_q), \dots, (x_{j+R-1}, \tilde{y}_q)\} / A \subseteq \mathcal{D}\}. \end{aligned}$$

See Figure 1 (b) for a graphical example.

The above procedure for the selection of the interpolation nodes at the normal lines and their corresponding sets \mathcal{S}_q is performed only once at the beginning of

4 Extrapolation

4.1 Motivation

Interpolation can produce large errors if there is a discontinuity in the region determined by the interpolation nodes and the evaluation point. When implementing extrapolation at ghost cells, as in Section 3, in order to avoid this considerable loss of precision or even a complete failure of the simulation, it is necessary to handle this situation carefully.

Since in our procedure the interpolator is evaluated at a point which is not necessarily centered with respect to the interpolation nodes, we cannot directly use techniques based on the partition of the stencil in substencils and/or the weighting of these, such as it is done in ENO [11] or WENO schemes, since in this case not all the substencils are useful, this depending on the localization of the discontinuity and the evaluation point.

Consider for instance the function $u := \chi_{[1/2, +\infty)}$ and take the nodes $x_i := i - 1$, $1 \leq i \leq 5$, with nodal values $u_i := u(x_i)$ and suppose we want to extrapolate this information at $x^* = -1$. Our nodal values are thus $u_1 = 0$ and $u_i = 1$ for $2 \leq i \leq 5$. It is well-known that the ENO3 technique divides the global stencil of five points into three substencils, $S_r := \{x_{r+1}, x_{r+2}, x_{r+3}\}$, $0 \leq r \leq 2$, and chooses the one with maximal smoothness in terms of its divided differences, in this case, S_1 or S_2 , both with all nodal values equal to 1 and thus all derivatives are zero. However, the result of this extrapolation at $x^* = 1$ is 1, which corresponds to the other state of the discontinuity from where x^* is located. The same applies for WENO.

Therefore, the interpolation strategy should be made more flexible, in order to choose certain nodes as valid according to some criterion and reject the rest. The strategy expounded in section 3 lets us focus on a one-dimensional setting.

4.2 Stencil selection by thresholding

Lets us assume that we have information on a stencil of not necessarily equispaced nodes, $x_1 < \dots < x_R$, with corresponding nodal values $u_i = u(x_i)$, and that we wish to interpolate at a certain node x^* .

The key node on which we establish a proximity criterion on its corresponding nodal value is the interior node which is the closest to x^* , i.e., we choose the node x_{i_0} , $i_0 \in \{1, \dots, R\}$ such that:

$$i_0 = \operatorname{argmin}_{1 \leq i \leq R} |x_i - x^*|.$$

Now, the goal is to approximate the value that that node should have, based on the information of the “smoothest” substencil and the node x_{i_0} .

Let M , $1 \leq M \leq R$, be the prescribed size for substencils. We therefore have $R - M + 1$ possible substencils:

$$S_r = \{x_{r+1}, \dots, x_{r+M}\}, \quad 0 \leq r \leq R - M.$$

We denote by $p_r(x)$ the interpolator associated to the stencil S_r , $0 \leq r \leq R - M$. If sufficient smoothness at the whole stencil holds, then one has:

$$u(x_i) - p_r(x_i) = \mathcal{O}(h_x^M), \quad i = 1, \dots, R, \quad (12)$$

therefore

$$u(x_i) = u(x_{i_0}) + (p_r(x_i) - p_r(x_{i_0})) + \mathcal{O}(h_x^M).$$

We select the substencil that solves:

$$r_0 := \underset{0 \leq r \leq R-M}{\operatorname{argmin}} \sum_{k=1}^{M-1} \int_{x_{r+1}}^{x_{r+M}} (x_{r+M} - x_{r+1})^{2k-1} p_r^{(k)}(x)^2 dx, \quad (13)$$

and define

$$v_i := u_{i_0} + (p_{r_0}(x_i) - p_{r_0}(x_{i_0})). \quad (14)$$

From (12), we have that $v_i = u_i + \mathcal{O}(h_x^M)$ if there's smoothness up to the $(M-1)$ -th derivative. On the other hand, assuming that u is smooth on an open set that contains S_{r_0} , if there is a discontinuity within the whole stencil $\bigcup_{r=0}^{R-M} S_r$ and u_i is quite far from u_{i_0} , since by construction $v_i = u_{i_0} + \mathcal{O}(h_x)$, then it can be expected that v_i also be quite different from u_i .

In order for the smoothness assumption on S_{r_0} to make sense in a general setting, one needs $M \leq E(\frac{R}{2})$, because all substencils would overlap in some common central nodes otherwise, leading to a situation where all substencils contain a discontinuity if it is contained in the overlapping region.

Therefore, one can conclude that the proximity of v_i with respect to u_i indicates the stencil smoothness that would entail including u_i in a hypothetical stencil for the final extrapolation.

Finally, let $\delta \in (0, 1]$ be a *threshold* and define the set of indexes

$$I_\delta := \{i \in \{1, \dots, R\} : \delta(|u_i - u_{i_0}| + D(x_i)) \leq |v_i - u_{i_0}| + D(x_i)\}, \quad (15)$$

where

$$D(x) := \sum_{j=1}^{M-1} \left| (x - x_{i_0})^j p_{r_0}^{(j)}(x_{i_0}) \right|.$$

Notice that $I_\delta \neq \emptyset$, since $i_0 \in I_\delta$.

The term $D(x_i)$ is used in (15) to avoid an order loss at smoothness regions whenever $\exists j_0, 1 \leq j_0 \leq M-1 : |u^{(j_0)}| \geq \mathcal{O}(\Delta x^M)$ near x_{i_0} . When the first derivative is close to zero, despite both $|v_i - u_{i_0}|$ and $|u_i - u_{i_0}|$ are still M -th order close, its quotient may be far from 1, specially when one of the previous expressions is close to be zero or even exactly zero (for instance, in zeros of even degree functions). The terms $D(x_i)$, alleviates this discrepancy by adding a $\mathcal{O}(h_x^{k_0}) \neq \mathcal{O}(h_x^{k_0+1})$ term, with $k_0 < M$, with k_0 the minimum index such that the k_0 -th derivative does not have a zero around x_{i_0} . The definitive stencil is the largest stencil in I_δ containing i_0 .

As last (optional) filter, if u^* is the value obtained from Lagrange interpolation from the resulting stencil, then the same threshold criterion can be applied to that value, resulting in the definitive extrapolation value:

$$u_{\text{def}}^* = \begin{cases} u^* & \text{if } \delta'(|u^* - u_{i_0}| + D(x^*)) \leq |p_r(x^*) - p_r(x_{i_0})| + D(x^*) \\ u_{i_0} & \text{if } \delta'(|u^* - u_{i_0}| + D(x^*)) > |p_r(x^*) - p_r(x_{i_0})| + D(x^*) \end{cases} \quad (16)$$

with $0 \leq \delta' \leq 1$.

This last criterion can be useful to detect wrong extrapolations (even when data are apparently smooth and previous criteria are met). Since it is an a posteriori

criterion, we may generally use it with threshold values that are more permissive, i.e., much smaller than one, than those for the nodes rejection. By construction, the closer the parameter δ is to one the lesser the tolerance to high gradients will be (with the consequent risk of eliminating some nodes from smooth regions). On the other hand, if δ is set too low, there may appear some oscillations or artifacts near discontinuities.

The quality of the smoothness criterion is enhanced with a larger substencil size (there is less risk of rejecting “correct” nodes). Furthermore a larger substencil can be also used to avoid a loss of precision order when consecutive derivatives are null at some point (precisely, until the $(M - 2)$ -th order derivative). Nevertheless, this would force increasing the size R of the global stencil, i.e., obtain more data from the general problem in order to avoid the previously mentioned problem.

In summary, the extrapolation of the nodal data $\{(x_i, u_i)\}_{i=1}^R$ to the point x^* consists of the following steps:

1. Find i_0 such that x_{i_0} is the closest node to x^* .
2. Find the M -point stencil $\mathcal{S}_{r_0} = \{x_{r_0+j}\}_{j=1}^M$ with maximal smoothness. We use the smoothness indicators in (13) for this purpose.
3. For $i \in \{1, \dots, R\}$ compute candidate approximations v_i of u_i using (14).
4. Fix a value $0 < \delta \leq 1$ and compute the set of nodes I_δ according to (15).
5. Extract the largest stencil in I_δ containing i_0 .
6. Compute the extrapolated value u^* at x^* using the stencil in the previous step.
7. Optionally, fix $0 < \delta' \leq 1$ and replace u^* by u_{def}^* computed from (16).

Let us apply the previous steps to the toy example in Section 4.1. We have $R = 5, M = 3$ in that example and we assume the values $\delta = \delta' = 0.5$, although any other choice of δ and δ' in the range $(0, 1)$ would give the same result. The stencil selection procedure is as follows:

1. The closest node to $x^* = -1$ is $x_1 = 0$, whose nodal value is $u_1 = 0$.
2. There are two stencils where the information is constant, S_1 and S_2 and therefore any of them would be selected in this step leading to the same result. Assume S_1 is chosen.
3. $v_i = u_1 = 0$ $1 \leq i \leq 5$ because $p_1 = 1$ for all $i \in \{1, \dots, 5\}$ and thus $D(x) = 0$.
4. The differences $|u_i - v_i|$ are all equal to 1 except for x_1 for which it is equal to 0. Therefore $I_\delta = \{x_1\}$ and the result of the extrapolation is $u^* = u_1 = 0$.
5. If the a posteriori filter is applied the result is kept as $\delta'|u^* - u_1| = 0 \leq 0 = |p_1(x^*) - p_1(x_1)|$.

In the numerical experiments that we will include in section 5, specially in problems with shocks, contacts and turbulence, there are occasions in which we will have to select more nodes than the minimum that would be needed to attain the order of the method. The reason for this decision is to yield more search room to locate a substencil with the maximal smoothness, for discontinuities propagate through several cells and one should compensate for this additional margin.

The well-posedness of the initial-boundary value problems depends heavily on the correct setting of boundary conditions. For linear systems and some nonlinear systems, it is well-known that boundary conditions on incoming characteristic variables (either globally or locally defined) should be obtained from prescribed boundary data (on primitive or conserved variables) and outgoing characteristic variables, in such a way that the number of incoming characteristics is the number

of boundary conditions (see [8, 9, 15] and references therein). This is the approach for setting numerical boundary conditions in general systems that has been used in [19, 20, 21]. In practice a formulation based on either conserved or primitive variables is preferred as long as the possible combinations of (conserved or primitive) variables to be determined by boundary conditions are known. For the Euler equations this equivalence is known and depends essentially on whether the flow is subsonic or supersonic and the kind of boundary conditions under consideration. We refer to [24, 16] for further details.

In the examples shown in section 5 we focus on the case of the Euler equations with reflecting boundary conditions on solid walls, at which the normal velocity is set to zero, thus only one characteristic is incoming. Furthermore, the value corresponding to this incoming characteristic can be obtained from the normal velocity (which is set to zero) and the other outgoing characteristics. This is consistent with our procedure for the 2D experiments, for which we use extrapolation on rotated primitive variables ρ, v^n, v^t, p (see Section 3.2 for the definition of v^n, v^t), using boundary data $v^n = 0$ on the solid walls.

On the other hand, when the flow is supersonic all characteristics are incoming at the inlet (inflow boundary) and outgoing at the outlet (outflow boundary) and therefore we fix all primitive variables at the inflow boundaries and none at the outlet. Therefore, depending on the type of boundary condition, some variables may be fixed to values determined by the boundary conditions at the boundary points, which are included in the stencil used for extrapolation. A proper node spacing for stability is ensured as described in Appendix B.

5 Numerical experiments

5.1 One-dimensional experiments

In this section we present some one-dimensional numerical experiments where both the accuracy of the extrapolation method for smooth solutions and its behavior in presence of discontinuities will be tested and analyzed.

Let us remark that for one-dimensional tests it is not necessary to develop a procedure as in the two-dimensional case described in Section 3, because one can set up initially a proper spacing between the nodes and perform a straight extrapolation at the ghost cells without having stability issues due to the presence of small-cut cells. However, to present accuracy and stability analysis in an easier setup, we perform the one-dimensional extrapolation explained in (10), (11), which directly corresponds to the two-dimensional extrapolation procedure that is proposed in this paper. This approach will illustrate that the accuracy order will still be the expected one in the smooth case and that the extrapolation method shows good performance in the non-smooth case.

5.1.1 Linear advection, C^∞ solution.

We start with a simple one-dimensional test case that will be used to illustrate the performance of the proposed method and also to analyze the importance and relative influence of some elements of the algorithm along the four examples detailed

below. The problem statement for this test is the same as in [20]. We consider the linear advection equation

$$u_t + u_x = 0, \quad \Omega := (-1, 1),$$

with initial condition given by $u(x, 0) = 0.25 + 0.5 \sin(\pi x)$ and boundary condition $u(-1, t) = 0.25 - 0.5 \sin(\pi(1+t))$, $t \geq 0$. We apply a numerical outflow condition at $x = 1$, where Dirichlet boundary conditions cannot be imposed due to the direction of propagation of the information.

It is immediately checked that the unique (smooth) solution to this problem is

$$u(x, t) = 0.25 + 0.5 \sin(\pi(x - t)).$$

Example 1. In order to numerically test the order of accuracy we perform tests at resolutions given by $n = 20 \cdot 2^j$ points, $j = 1, \dots, 5$. The cell centers are $x_j := -1 + (j + \frac{1}{2})h_x$, with $h_x := \frac{2}{n}$. We recall that the set of all cell centers which are interior to Ω is

$$\mathcal{D} := \{x_j : j \in \{0, \dots, n-1\}\}.$$

Since we use WENO5 reconstruction, we require 3 extra cells at each side of the boundary, where extrapolation from the interior will take place.

- $x = -1$: x_j , $-3 \leq j \leq -1$.
- $x = 1$: x_j , $n \leq j \leq n+2$.

We perform the one-dimensional extrapolation explained in (10), (11), which directly corresponds to the two-dimensional extrapolation procedure that is proposed in this paper.

Given that the ODE solver is third order accurate, in order to attain fifth order accuracy in the overall scheme, we need to select a time step given by $\Delta t = (\frac{2}{n})^{\frac{5}{3}}$, which corresponding Courant numbers $\Delta t/h_x = (2/n)^{2/3} \leq 1/20^{2/3}$.

Since the left boundary conditions are time dependent, we also have to take into account that a specific approximation is needed in each of the 3 stages in each RK3-TVD time step. In general, if the inflow condition is given by some function $g(t)$ which is at least twice continuously differentiable, we have to use the following values at the boundary to preserve third order accuracy [6]:

- First stage: $g(t_k)$.
- Second stage: $g(t_k) + \Delta t g'(t_k)$.
- Third stage: $g(t_k) + \frac{1}{2} \Delta t g'(t_k) + \frac{1}{4} \Delta t^2 g''(t_k)$.

Taking into account all the previous considerations, we execute the simulation until $t = 1$ for all the previously specified resolutions and we study the errors in the 1 and ∞ norms, together with the order deduced from them. We consider different modalities of boundary extrapolation: Constant extrapolation using only the closest node value (Table 1), five points stencil Lagrange extrapolation without discontinuity filters (Table 2) and with filters by thresholding for different choices of the thresholds (Tables 3–5).

The Table 1 illustrates that a low order extrapolation affects the order of the global scheme. We can see that in this case is downgraded to second order in $\|\cdot\|_1$, while it's first order in $\|\cdot\|_\infty$.

n	Error $\ \cdot\ _1$	Order $\ \cdot\ _1$	Error $\ \cdot\ _\infty$	Order $\ \cdot\ _\infty$
40	2.07E-3	—	3.87E-2	—
80	5.32E-4	1.96	1.96E-2	0.98
160	1.34E-4	1.99	9.81E-3	1.00
320	3.38E-5	1.99	4.91E-3	1.00
640	8.48E-6	1.99	2.45E-3	1.00

Table 1: Constant extrapolation (first order).

n	Error $\ \cdot\ _1$	Order $\ \cdot\ _1$	Error $\ \cdot\ _\infty$	Order $\ \cdot\ _\infty$
40	8.73E-6	—	2.44E-5	—
80	2.70E-7	5.01	7.35E-7	5.05
160	8.45E-9	5.00	2.31E-8	4.99
320	2.64E-10	5.00	6.95E-10	5.06
640	8.26E-12	5.00	2.13E-11	5.03

Table 2: Lagrange extrapolation (without filter).

n	Error $\ \cdot\ _1$	Order $\ \cdot\ _1$	Error $\ \cdot\ _\infty$	Order $\ \cdot\ _\infty$	% Success
40	5.45E-5	—	3.81E-4	—	86.18 %
80	3.06E-6	4.15	3.65E-5	3.38	95.77 %
160	1.34E-8	7.83	2.10E-7	7.44	99.55 %
320	2.64E-10	5.67	6.95E-10	8.93	100.00 %
640	8.26E-12	5.00	2.13E-11	5.03	100.00 %

Table 3: Filter for detection of discontinuities, $\delta = \delta' = 0.99$.

n	Error $\ \cdot\ _1$	Order $\ \cdot\ _1$	Error $\ \cdot\ _\infty$	Order $\ \cdot\ _\infty$	% Success
40	1.95E-5	—	1.38E-4	—	98.75 %
80	2.70E-7	6.17	7.35E-7	7.55	100.00 %
160	8.45E-9	5.00	2.31E-8	4.99	100.00 %
320	2.64E-10	5.00	6.95E-10	5.06	100.00 %
640	8.26E-12	5.00	2.13E-11	5.03	100.00 %

Table 4: Filter for detection of discontinuities, $\delta = 0.9$, $\delta' = 0.75$.

From Table 3 on, we add the last column with the percentage of extrapolations for which no rejection, either in the 5 nodes or in the final result in the a posteriori criterion, has taken place along the complete simulation.

From the results in those tables one can conclude that the detection behavior improves with increasing resolution. The technical reason for this is that the

n	Error $\ \cdot\ _1$	Order $\ \cdot\ _1$	Error $\ \cdot\ _\infty$	Order $\ \cdot\ _\infty$	% Success
40	8.73E-6	—	2.44E-5	—	100.00 %
80	2.70E-7	5.01	7.35E-7	5.05	100.00 %
160	8.45E-9	5.00	2.31E-8	4.99	100.00 %
320	2.64E-10	5.00	6.95E-10	5.06	100.00 %
640	8.26E-12	5.00	2.13E-11	5.03	100.00 %

Table 5: Filter for detection of discontinuities, $\delta = 0.75$, $\delta' = 0.5$.

quotient between the quantities appearing in (15) satisfies

$$\lim_{h_x \rightarrow 0} \frac{|u_i - u_{i_0}| + D(x_i)}{|v_i - u_{i_0}| + D(x_i)} = 1.$$

Even at low resolutions, we observe that it is sufficient to use a relatively restrictive threshold for not rejecting any point in the extrapolations procedure at each time step.

Example 2. We now perform a test omitting the $D(x_i)$ terms, which, as stated in the previous section, help avoiding erratic node eliminations when the differences are very close to be 0. The results can be seen at Table 6, illustrating the importance of such terms.

n	Error $\ \cdot\ _1$	Order $\ \cdot\ _1$	Error $\ \cdot\ _\infty$	Order $\ \cdot\ _\infty$	% Success
40	2.60E-5	—	1.72E-4	—	99.73 %
80	3.25E-7	6.32	1.60E-6	6.75	99.92 %
160	8.45E-9	5.27	2.31E-8	6.11	99.97 %
320	2.64E-10	5.00	6.95E-10	5.06	99.99 %
640	8.26E-12	5.00	2.13E-11	5.03	99.99 %

Table 6: Filter without $D(x_i)$ terms, $\delta = 0.2$, $\delta' = 0.1$.

We see that, indeed, without the $D(x_i)$ terms there are always some nodes removed even using very low threshold values.

Example 3. In order to illustrate the behaviour of our method in presence of small-cut cells, we now perform a test changing the location of the nodes by $x_j = -1 + (j + \frac{1}{8})h_x$ and following the procedure expounded in (10) and (11). For instance, to extrapolate data to $x_* := x_{-1} = -1 - \frac{7}{8}h_x$, one first computes $v = N(x_*) - x_* = -1 - x_{-1} = \frac{7}{8}h_x$, $C_x = E(v/h_x) = 1$ and considers points $N'_q = x_* + qC_x h_x = x_{-1} + qh_x = x_{q-1}$. Since there is a boundary condition at $N(x_*) = -1$, $N'_1 = x_0$ is not considered for extrapolation and the selected five nodes are $\{-1, N'_2, \dots, N'_5\} = \{-1, x_1, \dots, x_4\}$.

The results obtained for $\delta = 0.75$, $\delta' = 0.35$ are shown in Table 7. No node rejection occurred in this experiment.

n	Error $\ \cdot\ _1$	Order $\ \cdot\ _1$	Error $\ \cdot\ _\infty$	Order $\ \cdot\ _\infty$
40	9.81E-6	—	2.39E-5	—
80	3.06E-7	5.00	7.56E-7	4.98
160	9.52E-9	5.00	2.28E-8	5.05
320	2.97E-10	5.00	7.03E-10	5.02
640	9.23E-12	5.01	2.12E-11	5.06

Table 7: Lagrange extrapolation (node removal).

Note that in our numerical scheme and for accuracy reasons we have used $\Delta t = (h_x)^{\frac{5}{3}}$ and, therefore, no stability issue should appear anyway for big enough n . Forgetting about matching the spatial accuracy order with the time accuracy order, we set $n = 80$, $\Delta t = 0.9h_x$, that is, a CFL value of 0.9, and see that our scheme is indeed stable and obtains good results as can be seen in Figure 2.

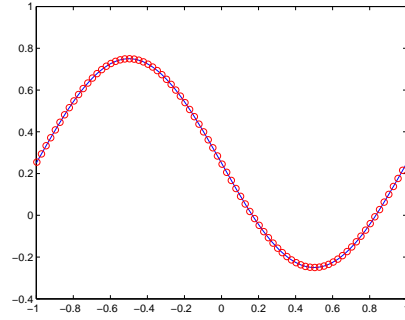


Fig. 2: Stability.

Example 4. To complete the previous examples we now analyze what happens if we attempt to extrapolate directly information at ghost cells without the removal of nodes too close to the boundary, i.e., for $x_* = x_{-1}$ the stencil would be $\{-1, x_0, \dots, x_3\}$. For this experiment, we use the grid from Example 3, a Courant number of 0.9, i.e., $\Delta t = 0.9h_x$, and a five nodes extrapolation at both sides of the boundary as done in the previous experiments. The crucial difference with respect to Example 3 is that now we do not remove N'_1 , thus resulting in a stability problem clearly visible already at the early stages of the simulation shown in Figure 3 (a), which ultimately lead to failure by numeric overflow.

In order to illustrate that it is actually a CFL issue, we now repeat the simulation with a Courant number set again to 0.9 but based on the distance of the closest node of the inflow boundary to this last one (based on a spacing of $\frac{h_x}{8}$), i.e., $\Delta t = 0.9\frac{h_x}{8}$. In Figure 3 (b) it can be seen that now the scheme is stable. We conclude that the intermediate step consisting in extrapolating the information on nodes with adequate spacing is necessary in order to avoid unnecessarily severe time step restrictions.

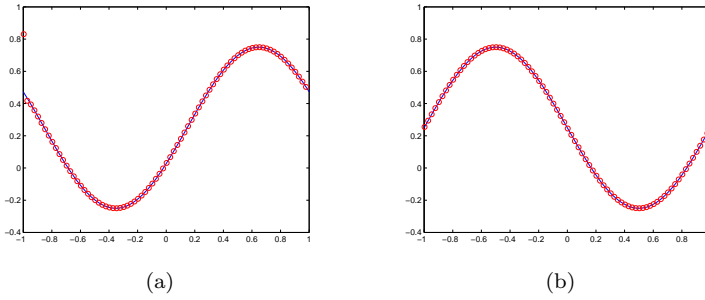


Fig. 3: (a) $\Delta t = 0.9h_x$, $t = 0.147$. Oscillations appear; (b) $\Delta t = 0.9\frac{h_x}{8}$, $t = 1$. No oscillations

5.1.2 Linear advection, discontinuous solution.

We illustrate with this experiment the behavior of the schemes when discontinuities are present and the entailed improvement with respect to using Lagrange extrapolation with no filters. We consider the same data as in the previous problem, but now the boundary condition is:

$$u(-1, t) = g(t) = \begin{cases} 0.25 & \text{if } t \leq 1 \\ -1 & \text{if } t > 1 \end{cases}$$

With this definition, the unique (weak) solution to this problem has a moving discontinuity and is given by:

$$u(x, t) = \begin{cases} -1 & \text{if } x < t - 2 \\ 0.25 & \text{if } t - 2 \leq x \leq t - 1 \\ 0.25 + 0.5 \sin(\pi(x - t)) & \text{if } x \geq t - 1 \end{cases}$$

In Figure 4 we check the graphical results that correspond to the simulation until $t = 1.5$, first using Lagrange extrapolation with no filters and afterwards with a filter with $\delta = 0.75$ and $\delta' = 0.5$, the same values that have achieved no node rejections in the first test. As it can be seen in Figure 4, Lagrange extrapolation without filters leads to spurious oscillations around the left side of the discontinuity, while thresholding removes them.

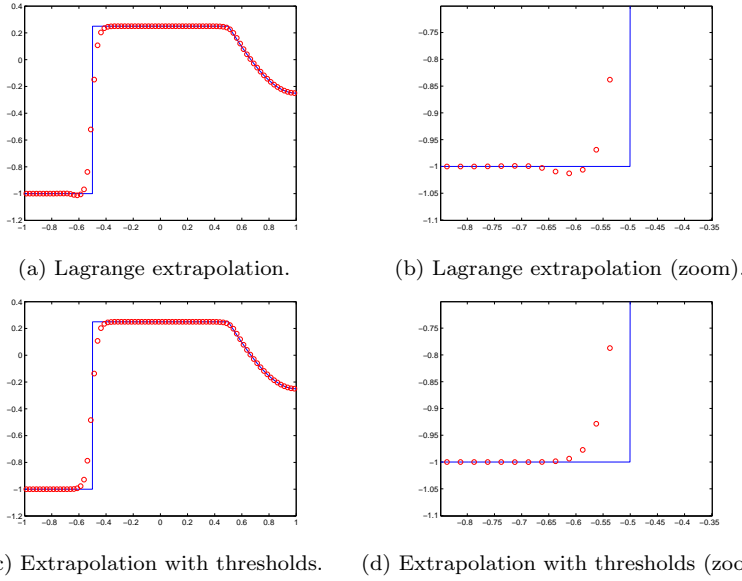


Fig. 4: Comparison of different extrapolations for the linear advection test with discontinuous solution.

5.1.3 Burgers equation.

Let's now perform some tests using Burgers equation

$$u_t + \left(\frac{u^2}{2} \right)_x = 0, \quad \Omega = (-1, 1),$$

with initial condition $u(x, 0) = 0.25 + 0.5 \sin(\pi x)$ with outflow condition at the right boundary and a left inflow boundary conditions given by $u(-1, t) = g(t)$, where $g(t) = w(-1, t)$, with w the exact solution of the problem using periodic boundary conditions.

For $t = 0.3$ the solution is smooth and we get the following error table for $n = 40 \cdot 2^k$, $0 \leq k \leq 5$, and the same spacing as the first test, using threshold values of $\delta = 0.75$ and $\delta' = 0.5$, where no node rejection occurs at any resolution.

n	Error $\ \cdot\ _1$	Order $\ \cdot\ _1$	Error $\ \cdot\ _\infty$	Order $\ \cdot\ _\infty$
40	3.66E-5	—	7.45E-4	—
80	6.96E-7	5.72	1.73E-5	5.43
160	1.33E-8	5.70	3.58E-7	5.59
320	3.34E-10	5.32	1.15E-8	4.96
640	1.02E-11	5.04	3.43E-10	5.06
1280	3.19E-13	4.99	1.03E-11	5.06

Table 8: Error table for Burgers equation, $t = 0.3$.

At $t = 1.1$, a shock is fully developed in the interior of the computational domain and enters the inflow boundary at $t = 8$. At $t = 12$ it is located at $x = 0$. We can see in Figure 5 that in this case the discontinuities are well captured by our scheme as well.

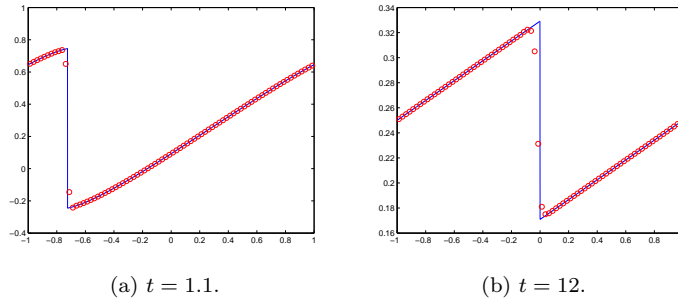


Fig. 5: Shock in Burgers equation, $n = 80$, $\delta = 0.75$, $\delta' = 0.5$.

5.1.4 Euler equations.

We end the one-dimensional experiments with an experiment using the Euler equations

$$\begin{aligned}
u_t + f(u)_x &= 0, \quad u = u(x, t), \quad \Omega = (0, 1), \\
u &= \begin{bmatrix} \rho \\ \rho v \\ E \end{bmatrix}, \quad f(u) = \begin{bmatrix} \rho v \\ p + \rho v^2 \\ v(E + p) \end{bmatrix},
\end{aligned} \tag{17}$$

where ρ is the density, v is the velocity and E is the specific energy of the system. The variable p stands for the pressure and is given by the equation of state:

$$p = (\gamma - 1) \left(E - \frac{1}{2} \rho v^2 \right),$$

where γ is the adiabatic constant, that will be taken as 1.4.

We simulate the interaction of two blast waves [22] by using the following initial data

$$u(x, 0) = \begin{cases} u_L & 0 < x < 0.1, \\ u_M & 0.1 < x < 0.9, \\ u_R & 0.9 < x < 1, \end{cases}$$

where $\rho_L = \rho_M = \rho_R = 1$, $v_L = v_M = v_R = 0$, $p_L = 10^3$, $p_M = 10^{-2}$, $p_R = 10^2$. We set reflecting boundary conditions at $x = 0$ and $x = 1$, simulating a solid wall at both sides. This problem involves multiple reflections of shocks and rarefactions off the walls and many interactions of waves inside the domain. We will use the same extrapolation nodes setup as in the previous tests as well as the same threshold values.

Figure 6 shows the density profile at $t = 0.038$ at two different resolutions, being the reference solution computed at a resolution of $\Delta x = 1/16000$. The figure clearly shows that the results are satisfactory.

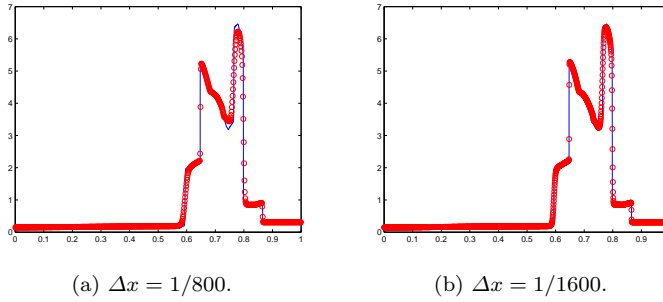


Fig. 6: Density profile, $t = 0.038$, $\delta = 0.75$, $\delta' = 0.5$.

5.2 Two-dimensional experiments

The equations that will be considered in this section are the two-dimensional Euler equations for inviscid gas dynamics

$$u_t + f(u)_x + g(u)_y = 0, \quad u = u(x, y, t),$$

$$u = \begin{bmatrix} \rho \\ \rho v^x \\ \rho v^y \\ E \end{bmatrix}, \quad f(u) = \begin{bmatrix} \rho v^x \\ p + \rho(v^x)^2 \\ \rho v^x v^y \\ v^x(E + p) \end{bmatrix}, \quad g(u) = \begin{bmatrix} \rho v^y \\ \rho v^x v^y \\ p + \rho(v^y)^2 \\ v^y(E + p) \end{bmatrix}. \quad (18)$$

In these equations, ρ is the density, (v^x, v^y) is the velocity and E is the specific energy of the system. The variable p stands for the pressure and is given by the equation of state:

$$p = (\gamma - 1) \left(E - \frac{1}{2} \rho((v^x)^2 + (v^y)^2) \right),$$

where γ is the adiabatic constant, that will be taken as 1.4 in all the experiments.

5.2.1 Double Mach Reflection

This experiment uses the Euler equations to model a vertical right-going Mach 10 shock colliding with an equilateral triangle. By symmetry, this is equivalent to a collision with a ramp with a slope of 30 degrees with respect to the horizontal line, which is how we will model the simulation to half the computational cost.

The data for this problem are the following:

$$\Omega = \left\{ (x, y) \in (0, 4) \times (0, 4) : y > \frac{\sqrt{3}}{3} \left(x - \frac{1}{4} \right) \right\}.$$

The domain with the corresponding boundary conditions is sketched in Figure 7

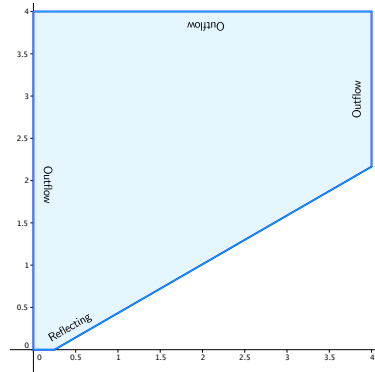


Fig. 7: Domain for the double Mach reflection test.

The initial conditions are the following:

$$\begin{aligned} u = (\rho, v^x, v^y, E) &= (8.0, 8.25, 0, 563.5) \text{ if } x \leq \frac{1}{4} \\ u = (\rho, v^x, v^y, E) &= (1.4, 0, 0, 2.5) \text{ if } x > \frac{1}{4} \end{aligned}$$

The most commonly used strategy for this simulation (see [22]) is to rotate the reference frame by -30 degrees, so that the simulation is cast into a rectangular domain, with a shock that is inclined 60 degrees with respect to the horizontal. In our case, we perform the simulation with the original problem to see that the improvement achieved by increasing the order of the extrapolations at the boundary leads to results that are comparable to those obtained with the rotated version.

Following the notation of the previous section, we have selected the values $R = 10$, $M = 3$ for the boundary (substencils are of the same size as those in WENO5). The reason for selecting $R = 10$ is not achieving an order higher than the one of the method, but having a wider stencil with more room for a safe selection of a substencil in smoothness regions.

We perform the simulation until $t = 0.2$. The experiment consists in different simulations with different threshold values, considering also a version with a unique point in the stencil (order 1). In Figure 8 we present the result for the density ρ at a resolution of $h_x = h_y = \frac{\sqrt{3}}{2} \frac{1}{640}$, which is equivalent to a resolution $\hat{h}_x = \hat{h}_y = \frac{1}{640}$ in the rotated experiment. A comparison of the results for the original and the rotated experiment for different extrapolation options is shown in Figure 9.

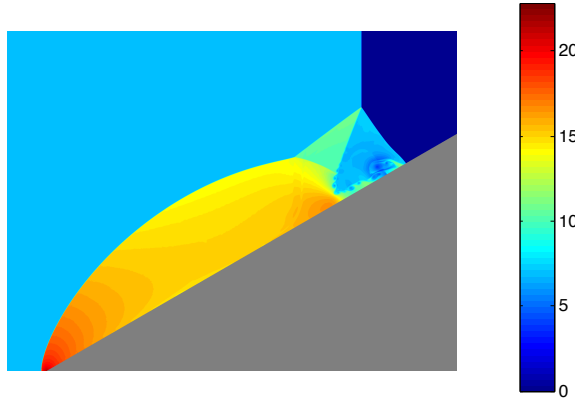


Fig. 8: Original problem.

The Schlieren plots shown in Figures 10, 11 and 12 display the gradients of the density field in an exponential scale in a gray scale, where darker tonalities correspond to higher values (see [14] and references therein for details).

As it can be seen, lower threshold values lead to better defined vortices. Also, note that according to the results on the figures, the rotated problem (with first order extrapolations) looks better than the original problem using also first order

extrapolations. One of the reasons might be the fact that the cell centers are exactly located on each normal line, leading to exact values on the first step of the extrapolation process (we recall the reader that this step consists in extrapolating information to points on normal lines from the values of the computational domain).

5.2.2 Interaction of a shock with a circular obstacle

We now change our data to a right-going vertical Mach 3 shock initially located at $x = 0.1$ with a circular obstacle with center $(0.5, 1)$ and radius 0.2 into a square domain $(0, 2) \times (0, 2)$. This experiment has already been performed in [4] using penalization techniques. To halve the computational time by exploiting the symmetry of the solution, we run a simulation until $t = 0.4$ and a mesh size of $h_x = h_y = \frac{1}{512}$ on the upper half of the domain, by adding reflecting boundary conditions at the bottom. A Schlieren plot of the result can be seen at Figure 11. As it can be seen, the results are very similar to those obtained in [4].

5.2.3 Interaction of a shock with multiple circular obstacles

We repeat the previous experiment by adding multiple circles in the domain as shown in Figure 12. This test can also be found in [4]. In this case, we run the simulation until $t = 0.5$ and a mesh size of $h_x = h_y = \frac{1}{512}$ on the whole domain. As in the previous experiment, we present a Schlieren plot for the last time step in Figure 12. These results are again consistent with those obtained in [4].

6 Conclusions and future work

In this paper we have presented some techniques for data extrapolation to handle boundary conditions for finite difference numerical methods for hyperbolic conservation laws. We have obtained some successful simulations in non rectangular domains. This illustrates that Lagrange extrapolation is a viable technique for filling-in auxiliary data at the ghost cells, as long as sufficient care is taken for accounting for possible discontinuities.

Furthermore, these techniques are designed to avoid an order loss at the boundary of complex domains in methods that require Cartesian meshes, a loss that can propagate to the rest of the data, thus notably decreasing the simulation quality. The results that have been obtained with these techniques entail an improvement that solves the previous problem without a significant increase in computational time at not excessively low resolutions.

The extrapolation techniques proposed in this paper have the advantage of letting a regulation of the tolerance to some variations at the boundary by using a threshold parameter. This, besides being data scale independent, is useful in simulations with strong turbulence or, in general, with wide regions where the data is not smooth. However, the need of tuning the thresholding parameters to the particular problem represents a drawback of the method.

Therefore, as future work we encompass studying the design of weighting methods, akin to WENO, that let performing extrapolations taking advantage of the

idea that has been used for extrapolation based on a threshold parameter, by assigning a convenient weight in each case, without needing a Boolean choice as in the case of using thresholds.

We are also regarding, on the other hand, the implementation of this methodology of boundary extrapolation techniques to Adaptive Mesh Refinement algorithms [2,3], trying not to excessively compromise their recognized efficiency on rectangular domains.

A Computations of intersections and normals for meshing

We have implemented a method to automatically compute the interior cells to Ω , the ghost cells and the normal (to $\partial\Omega$) vectors associated to them. We require a parametric definition of the curve described by $\partial\Omega$.

The knowledge of the Lipschitz constants of this curve is enough for computing the intersections of the boundary with the mesh lines. Indeed, with the notation $\alpha = (\alpha_x, \alpha_y) : [a, b] \rightarrow \mathbb{R}^2$ for the curve described by $\partial\Omega$, if L_x and L_y are upper bounds for the Lipschitz constants of the respective components of α , then the values $\Delta_x s := \frac{h_x}{L_x}$, $\Delta_y s := \frac{h_y}{L_y}$ satisfy

$$|\alpha_x(s + \Delta_x s) - \alpha_x(s)| \leq h_x \quad \forall s \in [a, b - \Delta_x s]$$

$$|\alpha_y(s + \Delta_y s) - \alpha_y(s)| \leq h_y \quad \forall s \in [a, b - \Delta_y s].$$

If we detect that a vertical or horizontal mesh line passes through two values of the parameter, we use Newton-Raphson's method, combined with bisection to safely approximate the intersection.

A similar strategy is used for the computations of the normals. In this case, given a ghost cell center, (x, y) , we start from the parameter value of the intersection that has generated that cell, s_0 , for this should not be far from the value of the parameter that corresponds to the point $N(x, y) \in \partial\Omega$ that determines the normal vector to the boundary passing by (x, y) .

Our search criterion is based on the sign of the scalar product of the tangent vector, $(\alpha'_x(s), \alpha'_y(s))$ and the vector formed by $(\alpha_x(s), \alpha_y(s))$ and (x, y) . At any rate, we aim to find s satisfying the equation

$$f(s) := \langle (\alpha'_x(s), \alpha'_y(s)), (\alpha_x(s) - x, \alpha_y(s) - y) \rangle = 0. \quad (19)$$

To accomplish this, we start from $s = s_0$ and evaluate this expression at points at each side of s_0 until a sign change in f is found. At this point we can use Newton-Raphson's method, together with bisection, to safely approximate the solution of (19) to the required precision.

B Linear stability analysis for inflow boundary conditions

Since a GKS stability analysis (see [10]) is out of the scope of this paper, we perform a simpler stability analysis to illustrate the strong influence of the spacing of the closest node to the boundary in the stability of the global numerical method.

For the sake of the exposition, we consider a linear advection equation

$$u_x + u_t = 0$$

defined on $\Omega = (0, 1)$ and inflow condition at $x = 0$, $u(0, t) = g(t)$. Let $h_x > 0$, $\Delta t > 0$, $k \in (0, 1]$ and define our grid points as $x_j := (k + j)h_x$, $0 \leq j \leq E(\frac{1}{h_x})$ and $t_n := n\Delta t$.

For solving numerically the equation, we use a first order upwind scheme:

$$U_j^{n+1} = U_j^n - \frac{\Delta t}{h_x} (U_j^n - U_{j-1}^n)$$

Assume we want to use linear interpolation at the boundary. This involves the inflow condition itself and the node U_0^n at each time step n . Naming $G^n := g(t_n)$, if we want to extrapolate at

$x_{-1} = (k-1)h_x$, where no information is available, at time step n using these two points, it can be shown by performing a linear extrapolation that

$$U_{-1}^n = \frac{1}{k}G^n + \frac{k-1}{k}U_0^n.$$

Since we want to focus on a stability analysis around the left boundary, where inflow conditions are prescribed, the scheme at x_0 reads

$$\begin{aligned} U_0^{n+1} &= U_0^n - \frac{\Delta t}{h_x}(U_0^n - U_{-1}^n) = U_0^n - \frac{\Delta t}{h_x}\left(U_0^n - \frac{1}{k}G^n + \frac{1-k}{k}U_0^n\right) = \\ &= \left(1 - \frac{\Delta t}{kh_x}\right)U_0^n + \frac{\Delta t}{kh_x}G^n = U_0^n - \frac{\Delta t}{kh_x}(U_0^n - G^n). \end{aligned}$$

With this, following a standard Von Neumann stability analysis from this new scheme, a necessary condition for stability is

$$0 \leq \frac{\Delta t}{kh_x} \leq 1,$$

which is equivalent to

$$k \geq \frac{\Delta t}{h_x} = \text{CFL}.$$

C Accuracy of schemes obtained from extrapolation at ghost cells

Related to Section 2.1, let us denote

$$\begin{aligned} \Phi(a_{-p-1}, \dots, a_q) &= \hat{f}(a_{-p}, \dots, a_q) - \hat{f}(a_{-p-1}, \dots, a_{q-1}) \\ U(h) &= (u(x - (p+1)h), \dots, u(x + qh)) \end{aligned}$$

for fixed x and sufficiently smooth u , \hat{f} . Then (5) is equivalent to

$$F(h) = \Phi(U(h)) = hf(u(x))_x + \mathcal{O}(h^{r+1}), \quad (20)$$

which is in turn equivalent to

$$F'(0) = f'(u(x))u'(x), \quad F^{(n)}(0) = 0, \quad n = 2, \dots, r. \quad (21)$$

If \hat{f} were a linear function, these relations would immediately yield a linear system of equations for its coefficients. In general, a more complicated formula equivalent to (21) can be obtained as follows: By induction on n the following vectorial version of Faà di Bruno's Formula [5] can be proved:

$$F^{(n)}(h) = \sum_{m=1}^n \sum_{p_1, \dots, p_m=1}^{n-m+1} \alpha_{p_1, \dots, p_m} \sum_{j_1, \dots, j_m=-p-1}^q \frac{\partial^m \Phi(U(h))}{\partial a_{j_1} \dots \partial a_{j_m}} U_{j_1}^{(p_1)}(h) \dots U_{j_m}^{(p_m)}(h), \quad (22)$$

for suitable and uniquely defined coefficients α_{p_1, \dots, p_m} . From (23) and the fact that $U_j^{(\nu)} = j^\nu u^{(\nu)}(x)$, for $j = -p-1, \dots, q$ and $\nu \geq 0$, we deduce that

$$\begin{aligned} F^{(n)}(0) &= \sum_{m=1}^n \sum_{p_l=1}^{n-m+1} \alpha_{p_1, \dots, p_m} \sum_{j_l=-p-1}^q \Phi^{(j_1, \dots, j_m)}(x) j_1^{p_1} \dots j_m^{p_m} u^{(p_1)}(x) \dots u^{(p_m)}(x), \\ \Phi^{(j_1, \dots, j_m)}(x) &= \frac{\partial^m \Phi}{\partial a_{j_1} \dots \partial a_{j_m}}(u(x), \dots, u(x)). \end{aligned} \quad (23)$$

For $n = 1$, (23) is satisfied with $\alpha_{p_1} = 1$:

$$F'(0) = \left(\sum_{j_1=-p-1}^q j_1 \frac{\partial \Phi}{\partial a_{j_1}}(u(x), \dots, u(x)) \right) u'(x).$$

It follows from (21) that $F'(0) = f'(u(x))u'(x)$ for any sufficiently smooth u if and only if

$$\sum_{j=-p-1}^q j \frac{\partial \Phi}{\partial a_j}(u(x), \dots, u(x)) = f'(u(x)),$$

i.e.,

$$\sum_{j=-p-1}^q j \frac{\partial \Phi}{\partial a_j}(u, \dots, u) = f'(u).$$

Now, (20) may be obtained by any means but, as we have just seen, they are equivalent to (21), (23), which only depends on derivatives of u at x , as long as u is smooth enough at a convex open set containing the corresponding stencil.

Assume now that that $u(x - (p+1)h)$ is replaced by, $\tilde{u}(x - (p+1)h)$, the evaluation at $x - (p+1)h$ of a polynomial that interpolates u at another stencil $x + p'h, \dots, x + q'h$, with $p' \geq -p$. Let us denote $\bar{q} = \max(q, q')$ and

$$\begin{aligned} V(h) &= (\tilde{u}(x - (p+1)h), u(x - ph), \dots, u(x + qh)) = W(u(x - ph), \dots, u(x + \bar{q}h)), \\ G(h) &= \Phi(V(h)). \end{aligned}$$

If u is smooth in a convex open set containing $[x - (p+1)h, \dots, x + \bar{q}h]$, then

$$u(x - (p+1)h) - \tilde{u}(x - (p+1)h) = \mathcal{O}(h^s), s \geq 2$$

and, therefore,

$$F(h) - G(h) = \frac{\partial \Phi(\xi_h)}{\partial a_{-p-1}}(u(x - (p+1)h) - \tilde{u}(x - (p+1)h)) = \mathcal{O}(h^s).$$

It then follows from (20) that

$$G(h) = hf(u(x))_x + \mathcal{O}(h^{r'+1}), r' = \min(r, s-1), \quad (24)$$

under the assumption of u being smooth in a convex open set containing $[x - (p+1)h, \dots, x + \bar{q}h]$. As argued above, this is equivalent to

$$G'(0) = f(u(x))_x, \quad G^{(n)}(0) = 0, \quad n = 2, \dots, r', \quad (25)$$

which translates into a functional relationship akin to that for F . But now G depends only on the stencil $x - ph, \dots, x + \bar{q}h$ and therefore (25) on u being smooth in a convex open set containing $[x - ph, \dots, x + \bar{q}h]$, i.e.,

$$\frac{G(h)}{h} = f(u(x))_x + \mathcal{O}(h^{r'})$$

if u is smooth in a convex open set containing $[x - ph, \dots, x + \bar{q}h]$.

Therefore, we have concluded that r -th order extrapolation applied to r -th order schemes decreases the order of the scheme near the boundaries to $r-1$. It can be seen that this order is sharp. This is in apparent contradiction with the results obtained in Section 5.1, where fifth order extrapolation applied together with fifth order schemes yields fifth order global errors, both in 1-norm and ∞ -norm.

We next justify that the global errors are of order r in 1-norm if the local error is of order $r+1$ at all but a bounded number (with respect to M) of nodes where the order is a unit less.

Let us denote $v_j^n = u(x_j, t_n)$, $j = 1, \dots, M$, for M the total number of spatial nodes, and $\mathcal{H} = \mathcal{H}_{\lambda, h}$, $\lambda = \Delta t/h$, the operator of the numerical scheme:

$$u^{n+1} = \mathcal{H}u^n, \quad \mathcal{H} : \mathbb{R}^M \rightarrow \mathbb{R}^M. \quad (26)$$

With this notation, the global error is $e^n = v^n - u^n$ and the local error can be written as $f_j^n = v_j^{n+1} - \mathcal{H}v_j^n$, which yields:

$$v^{n+1} = \mathcal{H}(v^n) + f^n. \quad (27)$$

Subtracting (26) and (27) and using the mean value theorem for \mathcal{H} we obtain a relationship between local and global error:

$$e^{n+1} = B_n e^n + f^n, \quad (28)$$

where

$$B_n = \int_0^1 \mathcal{H}'(u^n + s(v^n - u^n)) ds,$$

which, by induction on n , yields

$$e^n = \sum_{k=0}^{n-1} \left(\prod_{m=k+1}^{n-1} B_m \right) f^k. \quad (29)$$

Now, we recall that the classical argument to obtain convergence from consistency and stability proceeds as follows: Given some fixed $T > 0$, if for $h \in (0, h_0)$,

$$\|f^k\| \leq Ah^{r+1}, \quad \forall k \text{ such that } k\Delta t \leq T, \quad (30)$$

and, for the induced matrix norm, $\|B_m\| \leq 1 + Dh$, then it easily follows that $\|e^n\| \leq Ch^r$ for all $h \in (0, h_0)$ and all n such that $n\Delta t = n\lambda h \leq T$.

This analysis is sufficient for the 1-norm if a bounded number of nodes x_j satisfy $f_j^k = \mathcal{O}(h^r)$, whereas the rest satisfy $f_j^k = \mathcal{O}(h^{r+1})$, since then $\|f_j\|_1 = h \sum_{j=1}^M |f_j^k| = \mathcal{O}(h^{r+1})$. But this analysis does not explain that $\|e^n\|_\infty = \mathcal{O}(h^r)$, since in this case we have $\|f^k\|_\infty = \mathcal{O}(h^r)$, i.e., (30) does not hold, so this argument would yield $\|e^n\|_\infty = \mathcal{O}(h^{r-1})$. A finer analysis, based on the examination of the entries of the vectors involved in (29), is then needed to obtain $\|e^n\|_\infty = \mathcal{O}(h^r)$. The analysis of

$$e_p^n = \sum_{k=0}^{n-1} \sum_{q=1}^M \left(\prod_{m=k+1}^{n-1} B_m \right)_{pq} f_q^k, \quad (31)$$

can be quite involved in general and it is out of the scope of this work. We will show a particular case in which we obtain global errors of order 1 (in ∞ -norm) from local errors with some bounded number of entries of order 1 and the rest of order 2. We consider the upwind scheme

$$u_i^{n+1} = (1 - \lambda)u_i^n + \lambda u_{i-1}^n, \quad i = 1, \dots, M$$

for the linear advection equation $u_t + u_x = 0$ with time dependent boundary condition at $x = 0$, $u(0, t) = g(t)$. The value of $u_0^n \approx u(x_0, t_n)$ needs to be supplied according to this boundary condition. Prescribing $u_0^n = g(t_n) = u(0, t_n)$ gives a first order approximation of $u(x_0, t_n) = u(-h/2, t_n)$ and effectively yields a local error of order $r = 1$ at x_1 :

$$|f_1^n| = |u(h/2, t_n + \Delta t) - (1 - \Delta t/h)u(h/2, t_n) - \Delta t/hg(t_n)| \leq A_1 h,$$

whereas the rest of the entries of the local error satisfy

$$|f_j^n| \leq Ah^2, \quad j = 2, \dots, M,$$

i.e., are of order $r + 1 = 2$, for suitable positive constants A_1, A .

For this linear case, all the matrices B_m are $(1 - \lambda)I_M + \lambda N_M$, where $N = N_M$ is the nilpotent matrix whose powers are given by $(N^j)_{pq} = \delta_{p-q, j}$, $j \geq 1$, $1 \leq p, q \leq M$. We

compute now, with the change of variables $k' = n - k - 1 \rightarrow k$:

$$\begin{aligned}
e_p^n &= \sum_{k=0}^{n-1} \sum_q^M ((1-\lambda)I + \lambda N)_{pq}^{n-k-1} f_q^k \\
&= \sum_{k=0}^{n-1} \sum_{q=1}^M \sum_{j=0}^{n-k-1} \binom{n-k-1}{j} (1-\lambda)^{n-k-1-j} \lambda^j N_{pq}^j f_q^k \\
&= \sum_{k=0}^{n-1} \sum_{q=1}^M \sum_{j=0}^{n-k-1} \binom{n-k-1}{j} (1-\lambda)^{n-k-1-j} \lambda^j \delta_{p-q,j} f_q^k \\
&= \sum_{k=0}^{n-1} \sum_{q=\max(1, p-n+k+1)}^p \binom{n-k-1}{p-q} (1-\lambda)^{n-k-1-p+q} \lambda^{p-q} f_q^k \\
&= \sum_{k=0}^{n-1} \sum_{q=\max(1, p-k)}^p \binom{k}{p-q} (1-\lambda)^{k-p+q} \lambda^{p-q} f_q^{n-k-1} \\
&= \sum_{q=1}^p \left(\lambda^{p-q} \sum_{k=p-q}^{n-1} \binom{k}{p-q} (1-\lambda)^{k-p+q} \right) f_q^{n-k-1}.
\end{aligned}$$

We can bound

$$\lambda^s \sum_{k=s}^{n-1} \binom{k}{s} (1-\lambda)^{k-s} \leq \lambda^s \sum_{k=s}^{\infty} \binom{k}{s} (1-\lambda)^{k-s}$$

for $s = p - q$ and use that $\lambda^s \sum_{k=s}^{n-1} \binom{k}{s} (1-\lambda)^{k-s} \leq \lambda^s \sum_{k=s}^{\infty} \binom{k}{s} (1-\lambda)^{k-s} = \frac{1}{\lambda}$ (see next lemma) to conclude:

$$|e_p^n| \leq \frac{1}{\lambda} \sum_{q=1}^p |f_q^{n-k-1}| \leq \frac{1}{\lambda} (A_1 h + (p-1) A h^2) \leq \frac{1}{\lambda} (A_1 h + M A h^2) = \frac{A_1 + A}{\lambda} h,$$

for any $p = 1, \dots, M$, i.e., $\|e^n\|_{\infty} = \mathcal{O}(h^r)$, $r = 1$, as proposed.

Lemma 1 For any $\lambda \in (0, 1)$ and $s \in \mathbb{N}$,

$$\sum_{k=s}^{\infty} \binom{k}{s} (1-\lambda)^{k-s} = \lambda^{-s-1}.$$

Proof Set $A_s = \sum_{k=s}^{\infty} \binom{k}{s} (1-\lambda)^{k-s}$. From the identity $\binom{k}{s} = \binom{k-1}{s} + \binom{k-1}{s-1}$, for $0 \leq s < k$, and the change of variables $k' = k - 1$ we get:

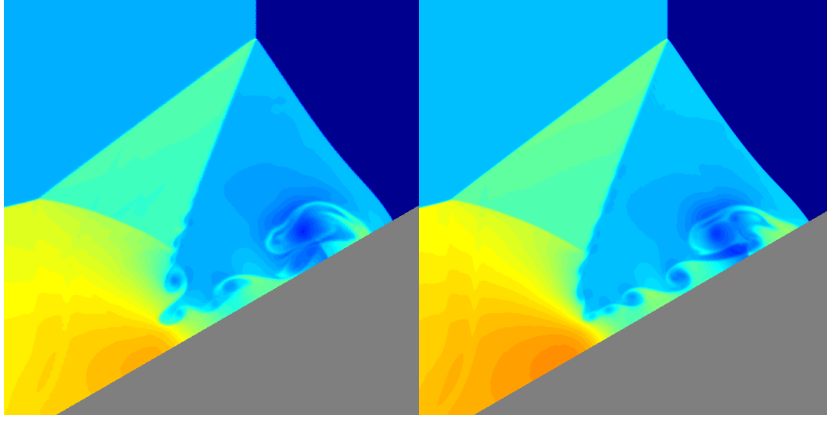
$$\begin{aligned}
\sum_{k=s}^{\infty} \binom{k}{s} (1-\lambda)^{k-s} &= 1 + \sum_{k=s+1}^{\infty} \left(\binom{k-1}{s} + \binom{k-1}{s-1} \right) (1-\lambda)^{k-s} \\
&= 1 + \sum_{k=s+1}^{\infty} \binom{k-1}{s} (1-\lambda)^{k-s} + \sum_{k=s+1}^{\infty} \binom{k-1}{s-1} (1-\lambda)^{k-s} \\
&= 1 + (1-\lambda) \sum_{k'=s}^{\infty} \binom{k'}{s} (1-\lambda)^{k'-s} + \sum_{k'=s}^{\infty} \binom{k'}{s-1} (1-\lambda)^{k'-s} \\
&= (1-\lambda) \sum_{k'=s}^{\infty} \binom{k'}{s} (1-\lambda)^{k'-s} + \sum_{k'=s-1}^{\infty} \binom{k'}{s-1} (1-\lambda)^{k'-s}.
\end{aligned}$$

We obtain that $A_s = (1-\lambda)A_s + A_{s-1}$ i.e., $A_s = \lambda^{-1}A_{s-1}$, which immediately yields

$$A_s = \lambda^{-s} A_0 = \lambda^{-s} \sum_{k=0}^{\infty} (1-\lambda)^k = \lambda^{-s-1}.$$

References

1. Aràndiga, F., Baeza, A., Belda, A.M., Mulet, P.: Analysis of WENO schemes for full and global accuracy. *SIAM J. Numer. Anal.* **49**(2), 893–915 (2011)
2. Baeza, A., Mulet, P.: Adaptive mesh refinement techniques for high-order shock capturing schemes for multi-dimensional hydrodynamic simulations. *Int. J. Numer. Meth. Fluids* **52**, 455–471 (2006)
3. Berger, M.J., Colella, P.: Local adaptive mesh refinement for shock hydrodynamics. *J. Comput. Phys.* **82**, 64–84 (1989)
4. Boiron, O., Chiavassa, G., Donat, R.: A high-resolution penalization method for large Mach number flows in the presence of obstacles. *Computers & Fluids* **38**, 703–714 (2009). DOI 10.1016/j.compfluid.2008.07.003
5. Faà di Bruno, C.F.: Note sur un nouvelle formule de calcul différentiel. *Quart. J. Math.* **1**, 359–360 (1857)
6. Carpenter, M., Gottlieb, D., Abarbanel, S., Don, W.S.: The theoretical accuracy of Runge-Kutta time discretizations for the initial boundary value problem: a study of the boundary error. *SIAM J. Sci. Comput.* **16**, 1241–1252 (1995)
7. Donat, R., Marquina, A.: Capturing shock reflections: An improved flux formula. *J. Comput. Phys.* **125**, 42–58 (1996)
8. Godlewski, E., Raviart, P.A.: Numerical approximation of hyperbolic systems of conservation laws, *Applied Mathematical Sciences*, vol. 118. Springer-Verlag, New York (1996). DOI 10.1007/978-1-4612-0713-9. URL <http://dx.doi.org/10.1007/978-1-4612-0713-9>
9. Gustafsson, B., Kreiss, H.O., Oliger, J.: Time dependent problems and difference methods. *Pure and Applied Mathematics* (New York). John Wiley & Sons, Inc., New York (1995). A Wiley-Interscience Publication
10. Gustafsson, B., Kreiss, H.O., Sundström, A.: Stability theory of difference approximations for mixed initial boundary value problems. II. *Math. Comp.* **26**, 649–686 (1972)
11. Harten, A., Engquist, B., Osher, S., Chakravarthy, S.R.: Uniformly high order accurate essentially non-oscillatory schemes, III. *J. Comput. Phys.* **71**(2), 231–303 (1987)
12. Huang, L., Shu, C.W., Zhang, M.: Numerical boundary conditions for the fast sweeping high order WENO methods for solving the Eikonal equation. *J. Comp. Math.* **26**, 336–346 (2008)
13. Jiang, G.S., Shu, C.W.: Efficient implementation of Weighted ENO schemes. *J. Of Comput. Phys.* **126**, 202–228 (1996)
14. Marquina, A., Mulet, P.: A flux-split algorithm applied to conservative models for multi-component compressible flows. *J. Comput. Phys.* **185**, 120–138 (2003)
15. Oliger, J., Sundström, A.: Theoretical and practical aspects of some initial boundary value problems in fluid dynamics. *SIAM J. Appl. Math.* **35**(3), 419–446 (1978)
16. Pletcher, R.H., Tannehill, J.C., Anderson, D.: *Computational fluid mechanics and heat transfer*, third edn. CRC Press (2012)
17. Shu, C.W., Osher, S.: Efficient implementation of essentially non-oscillatory shock-capturing schemes. *J. Comput. Phys.* **77**, 439–471 (1988)
18. Shu, C.W., Osher, S.: Efficient implementation of essentially non-oscillatory shock-capturing schemes, II. *J. Comput. Phys.* **83**(1), 32–78 (1989)
19. Sjogreen, B., Petersson, N.: A cartesian embedded boundary method for hyperbolic conservation laws. *Commun. Comput. Phys.* **2**, 1199–1219 (2007)
20. Tan, S., Shu, C.W.: Inverse Lax-Wendroff procedure for numerical boundary conditions of conservation laws. *J Comput. Phys.* **229**, 8144–8166 (2010)
21. Tan, S., Wang, C., Shu, C.W., Ning, J.: Efficient implementation of high order inverse Lax-Wendroff boundary treatment for conservation laws. *J. Comput. Phys.* **231**(6), 2510–2527 (2012)
22. Woodward, P., Colella, P.: The numerical simulation of two-dimensional fluid flow with strong shocks. *J. Comput. Phys.* **54**, 115–173 (1984)
23. Xiong, T., Zhang, M., Zhang, Y.T., Shu, C.W.: Fast sweeping fifth order WENO scheme for static Hamilton–Jacobi equations with accurate boundary treatment. *J. Sci. Comput.* **45**, 514–536 (2010)
24. Yee, H.C.: Numerical approximation of boundary conditions with applications to inviscid equations of gas dynamics. Tech. Rep. N81-19834, NASA (1981)



(a) Rotated domain.

(b) 1st o. extrapolations.

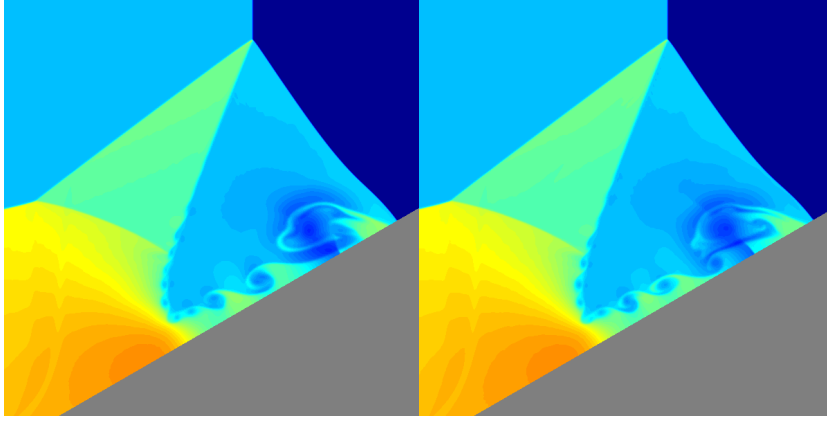
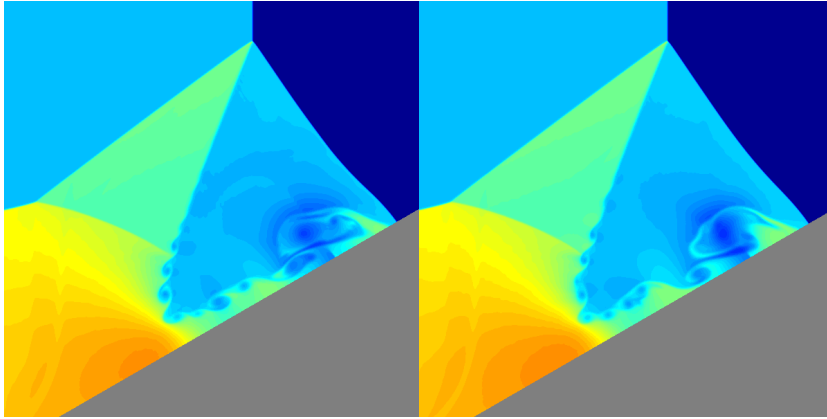
(c) 5th o. extrapolations. $\delta = \delta' = 0.9$.(d) 5th o. extrapolations. $\delta = \delta' = 0.5$.(e) 5th o. extrapolations. $\delta = \delta' = 0.35$.(f) 5th o. extrapolations. $\delta = \delta' = 0.2$.

Fig. 9: Enlarged view of the turbulence zone.

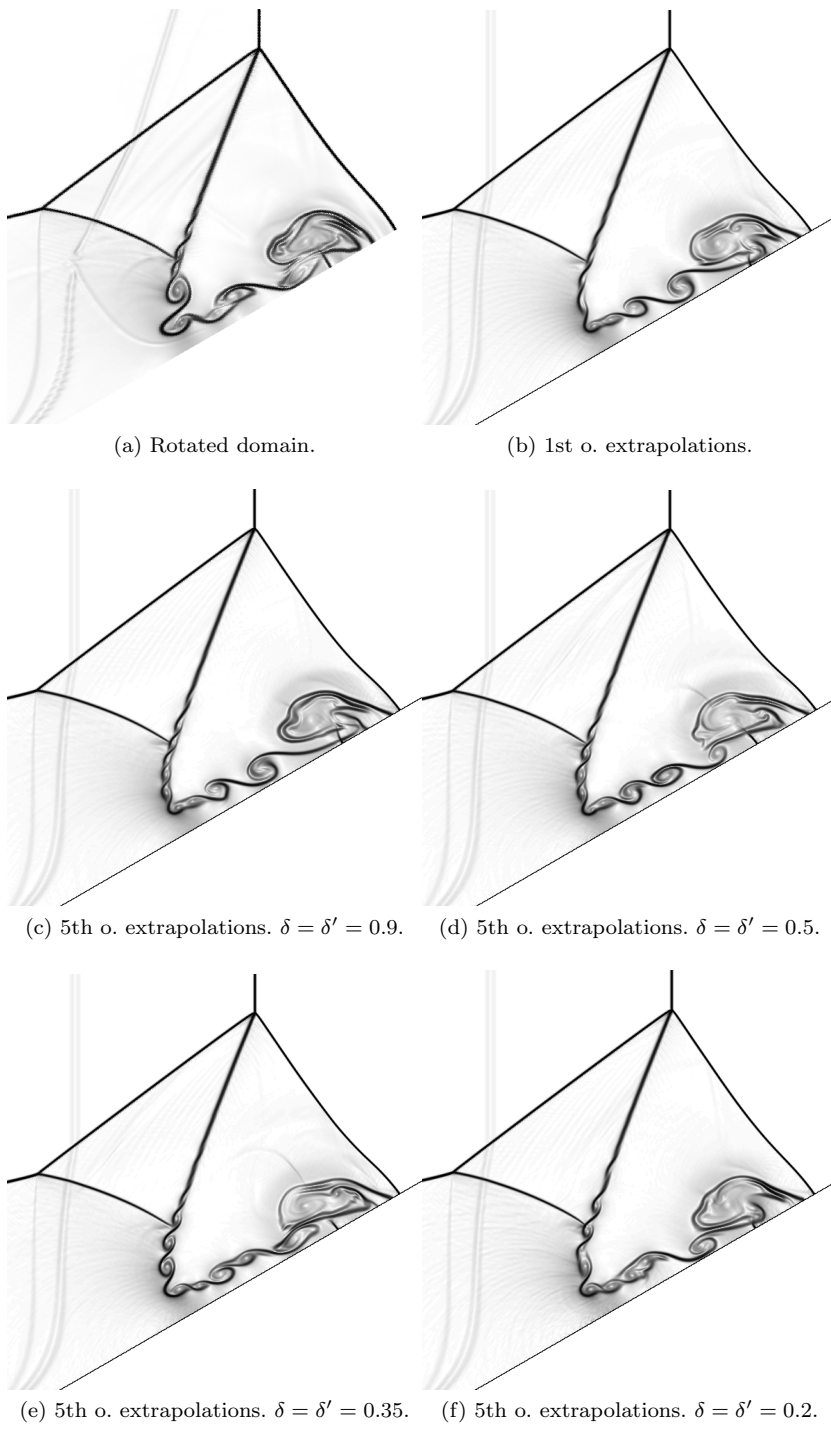


Fig. 10: Enlarged view of the turbulence zone (Schlieren).

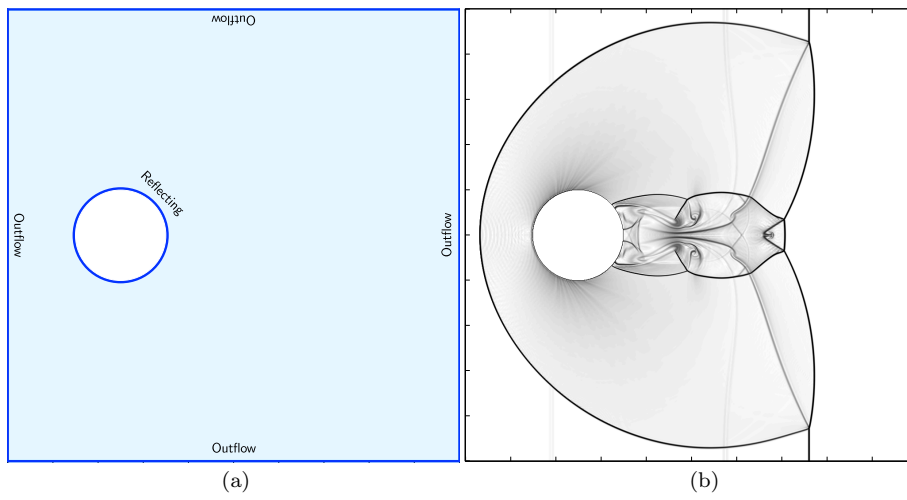


Fig. 11: Circle reflection test: (a) domain; (b) simulation for $t = 0.4$.

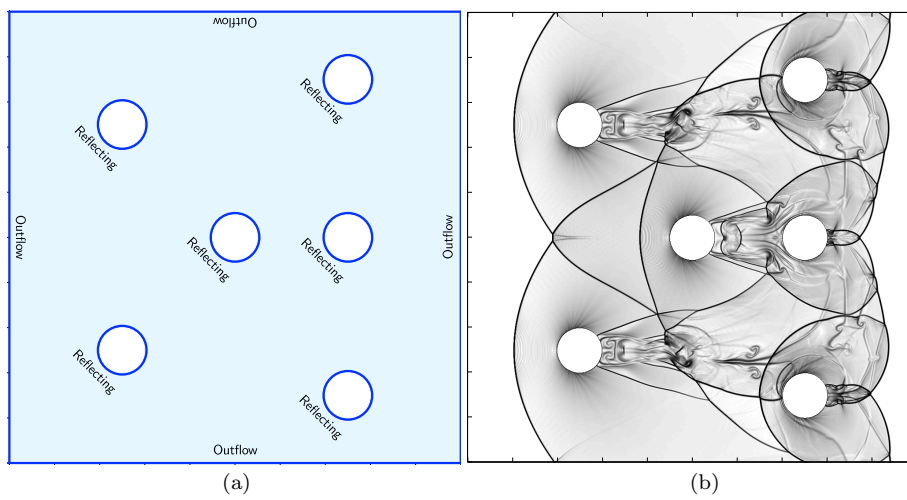


Fig. 12: Circles reflection test: (a) domain; (b) simulation for $t = 0.5$.